

# $B_0$ Mapping With Multi-Channel RF Coils at High Field

Simon Robinson<sup>1,2</sup> and Jorge Jovicich<sup>1,3\*</sup>

Mapping the static magnetic field via the phase evolution over gradient echo scans acquired at two or more echo times is an established method. A number of possibilities exist, however, for combining phase data from multi-channel coils, denoising and thresholding field maps for high field applications. Three methods for combining phase images when no body/volume coil is available are tested: (i) Hermitian product, (ii) phase-matching over channels, and (iii) a new approach based on calculating separate field maps for each channel. The separate channel method is shown to yield field maps with higher signal-to-noise ratio than the Hermitian product and phase-matching methods and fewer unwrapping errors at low signal-to-noise ratio. Separate channel combination also allows unreliable voxels to be identified via the standard deviation over channels, which is found to be the most effective means of denoising field maps. Tests were performed using multichannel coils with between 8 and 32 channels at 3 T, 4 T, and 7 T. For application in the correction of distortions in echo-planar images, a formulation is proposed for reducing the local gradient of field maps to eliminate signal pile-up or swapping artifacts. Field maps calculated using these techniques, implemented in a freely available MATLAB toolbox, provide the basis for an effective correction for echo-planar imaging distortions at high fields. *Magn Reson Med* 66:976–988, 2011. © 2011 Wiley-Liss, Inc.

**Key words:** field map; distortion correction; multichannel coil; 3 T; 4 T; 7 T

Spatial encoding in MRI is predicated on the local magnetic field being determined by applied gradient fields. In practice, differing tissue susceptibilities introduce regional variations in the static magnetic field ( $B_0$ ), and these lead to signal mislocalization, particularly in echo-planar imaging (EPI). Local deviations from  $B_0$  can be calculated from the evolution of phase between two or more gradient echoes, allowing the correction of distortion in EPI (1). While  $B_0$  mapping is a well-established technique for imaging with volume radio frequency (RF) coils at low and intermediate field strengths ( $\leq 3$  T), the

method used to combine phase images from multichannel RF coils needs consideration, and a number of confounds can lead to inaccuracies in field maps which compromise the quality of corrections, particularly at high static magnetic field and in regions of high susceptibility gradients.

The long readout train in EPI equates to a low bandwidth per pixel in the phase-encode direction, making EPI particularly prone to signal mislocalization along the phase-encode axis. Deviations from  $B_0$  are of relatively low spatial frequency, causing signal mislocalization to manifest as distortion in the image. Knowledge of local deviations from  $B_0$ , the field map, allows these distortions to be corrected (1). A number of other methods have been developed for the correction of distortions in EPI. The point-spread function method, for instance, has the advantage that the correction maps are subject to the same distortion from concomitant gradients as the EPI to be corrected (2,3) but is prone to artifacts close to the ventricles due to cerebrospinal fluid flow (4). More recent innovations, phase labeling for additional coordinate encoding (5) and phase labeling using sensitivity encoding (6) allow correction of both distortion and Nyquist ghosts. These methods are not widely implemented, however, and can be computationally demanding in reconstruction or correction, and if implemented on-console can be difficult to modify post-hoc—e.g., in case of movement between the acquisition of the reference scan and EPI. Field mapping has the benefit not only of the near universal availability of suitable MR methods (gradient-echo), but also of utility in other applications, such as the assessment of the effectiveness of shimming methods and use in calculating Blood Oxygen Level-Dependent sensitivity in single subjects (7).

It is increasingly common to use phased arrays of RF coils, particularly at high field, to increase signal-to-noise ratio (SNR) and allow parallel imaging (8,9). Combining phase images from these elements, which are generally subject to different and spatially varying phase offsets, is, however, nontrivial (10–12). Simple reconstruction methods commonly used for magnitude images, such as the sum-of-squares of the separate channels, generally lead to some degree of signal cancellation due to channel-specific phase offsets. On systems equipped with a body coil (most up to 3 T), field maps may be acquired with this to avoid having to combine phase images from the phased array elements. However, many high field (>3 T) systems do not have a body coil or other volume receive coil.

The principal problem with combining phase data from a number of RF coils is that each coil is subject to a different, spatially varying phase offset. Phase images are optimally combined using complex sensitivity maps measured via reference to volume coil measurements (12). In the absence of a volume reference, the three-

<sup>1</sup>Functional Neuroimaging Laboratory, Center for Mind/Brain Sciences (CIMEC), University of Trento, Mattarello, Italy.

<sup>2</sup>High Field MR Center of Excellence, Department of Radiology, Medical University of Vienna, Austria.

<sup>3</sup>Department of Cognitive and Education Sciences, University of Trento, Mattarello, Italy.

Grant sponsors: Government of the Autonomous Province of Trentino, Italy, Fondazione Cassa di Risparmio di Trento e Rovereto, University of Trento, Italy, and the Vienna Advanced Clinical Imaging Center (VIACLIC) project, funded by the Vienna Spots of Excellence Program of the Center of Innovation and Technology, City of Vienna (ZIT), Austria.

\*Correspondence to: Jorge Jovicich, Ph.D., Functional Neuroimaging Laboratory, Center for Mind/Brain Sciences, Via delle Regole 101–38060, Mattarello (TN), Italy. E-mail: jorge.jovicich@unitn.it

Received 9 June 2010; revised 15 January 2011; accepted 24 January 2011.

DOI 10.1002/mrm.22879

Published online 23 May 2011 in Wiley Online Library (wileyonlinelibrary.com).

dimensional distribution of phase offsets can be measured using a dual-echo scan (13), or estimated as a scalar derived from an overlapping reference region (10), and subtracted. In difference imaging applications such as field mapping, phase offsets are removed by calculation of difference images, e.g., using the Hermitian product (HP) method (14). The HP method has been compared with sensitivity encoding (SENSE), but not with phase matching, or other approaches that do not require a volume coil. Several other approaches have been proposed to combine phases in multichannel coils for structural phase imaging (15–17). These methods, which are optimized for phase contrast at high spatial resolution, are often based on phase-sensitive combination of individual coil data which generally depends on measured or estimated sensitivity profiles.

With an inherent encoding range limited to  $2\pi$ , phase images contain discontinuities or “wraps.” These may be identified via either their distribution in space (18,19) or discontinuities in the phase evolution over time (20–22). For the relatively low spatial resolution required for field mapping for distortion correction of EPI, a number methods offer sufficiently fast, robust correction (18,19,22). However, the automatic selection of seed voxels in two-dimensional (2D) spatial unwrapping often leads to an integer number of  $2\pi$  phase offsets between unwrapped slices and between echoes, which need to be identified and removed.

As difference images, field maps are also prone to noise, particularly at the image periphery and in regions of signal loss—both areas where reliable field map values are important. Spatial filtering methods such as three-dimensional Gaussian filtering (23) and 2D median filtering (3) have been proposed to smooth field maps at brain edges and in regions with low SNR. Denoising via the variation in voxel values over coil channels is tested here.

Finally, if used in distortion correction, field map values are converted to the voxel shifts required to remove distortions. If the gradient in this remapping process exceeds a certain value then conflicts arise, with signal “piling up” or being swapped over boundaries, which manifests as streaks, voids and rings in corrected images. While spatial smoothing reduces voxel shift gradients to some extent, it will not generally preclude the occurrence of this artifact, and an explicit voxel shift gradient thresholding is required. A subpixel-interpolation method has been proposed to address these remapping artifacts in a different distortion correction approach, based on the use of multiple EPI acquisitions with different  $k$ - $t$  space coverage (phase labeling for additional coordinate encoding) (5). To our knowledge, a solution has yet to be proposed for distortion correction with field maps. The problems described occur particularly at high static magnetic field strength and many are addressed here for the first time.

We compare two existing methods for combining phase images from multi-element coils for the creation of field maps—the HP (24) and phase matching methods (10)—and suggest a third, based on the calculation of separate field maps from each channel. Errors may occur in unwrapping phase images at low SNR, as is common in regions of high field gradients in gradient echo

images, high-resolution acquisitions for  $T_2^*$  mapping (25,26), and contrast-enhanced susceptibility-weighted imaging with the contrast agent superparamagnetic Iron Oxide (SPIO) (27). The extent to which these three methods are affected by unwrapping errors at low SNR is assessed in a phantom study and in in vivo data to which noise was added. A simple and effective means to identify and correct the occurrence of an integer number of  $2\pi$  phase jumps between slices and echoes is proposed, and a method for denoising field maps, based on the variation of field map values over channels, is assessed. Applying field maps to the correction of EPI distortion, we identify the criterion for the maximum remappable distortion and demonstrate how field maps may be rescaled in regions of high gradient to remove local artifacts while maintaining effective correction elsewhere. These solutions have been implemented as a freely available field mapping toolbox for MATLAB (MathWorks Inc, Natick, MA).

## MATERIALS AND METHODS

The main evaluation of different  $B_0$  mapping methods with phased arrays was performed with a group of seven subjects and phantom data measured with a 4 T MRI system and an 8-channel receiver coil. The  $B_0$  mapping methods were also tested on a 3 T and a 7 T system and with coils with other numbers of channels: a 32-channel at 3 T and 8-channel, 24-channel, and 32-channel coils at 7 T. These additional data were only acquired on one subject to test the applicability of field-mapping methods to various hardware configurations.

In spin-echo EPI, refocusing of susceptibility-induced dephasing reduces signal loss (at the cost of some functional sensitivity (28–30)) but does not alleviate signal mislocalization. The evaluation of  $B_0$  mapping methods considered both spin-echo (SE)-EPI and gradient-echo (GE)-EPI, receiver bandwidths, and time-series in the presence of motion to examine intersubject variability and applicability in a range of EPI variants and parameters (23). All subjects had no history of neurological or psychiatric disease and participated with written consent in the studies, which were approved by the Ethics Committees of the respective universities (4 T; the University of Trento, 3 T and 7 T; the Medical University of Vienna).

### Data Acquisition, 4 T

Seven subjects aged between 21 and 39 years, mean  $30 \pm 7$  years, participated with informed written consent in this part of the study. MRI were acquired with a 4 T Bruker Medspec scanner (Bruker Medical, Ettlingen, Germany) using a birdcage-transmit, 8-channel receive head coil (USA Instruments, Inc., Ohio). Field mapping was performed with a dual-echo (echo time (TE) = 6, 10 ms) GE sequence with pulse repetition time (TR) = 400 ms, flip angle (FA) =  $39^\circ$  (Ernst angle for grey matter at 4 T), pixel bandwidth = 260 Hz and fat saturation (20 oblique axial slices aligned parallel to the line connecting the anterior and posterior commissures (ACPC) of 2 mm thickness and

with 0.3 mm gap,  $128 \times 128$  matrix, field of view 256 mm). Phase and magnitude data were saved from each channel. Single-instance GE-EPIs and SE-EPIs were acquired with an effective echo time of 39 ms, TR = 5.6 s, and the same geometry, with the following receiver bandwidths, to generate the full range of distortions that may be realistically encountered at 4 T; 1056, 1086, 1116, 1150, 1184, 1220, 1260, 1302, 1346, 1396, 1446, 1502, 1562, 1628, 1698, 1776, 1860, and 1954 Hz/pixel, corresponding to phase encode bandwidths in the range 7.6 to 13.5 Hz. A matching single-echo GE anatomical reference scan was acquired (TE = 39 ms) to yield an image with similar contrast to the EPIs but with no distortion along the phase-encoding (PE) direction. For the phantom study of phase unwrapping errors at low SNR, dual-echo GE scans were acquired as above with FA =  $1^\circ$ . Time-series data (NR = 30) were also acquired with receiver bandwidth (RBW) = 1396 Hz/pixel, with GE-EPI and SE-EPI with the subject instructed to (i) remain as still as possible and (ii) move the head slowly about the left-right axis (a commonly observed, attention-related head motion in fMRI experiments).

#### Data Acquisition, 3 T

Measurements were made with a single 26-year-old male subject with a 3 T Siemens Magnetom TIM TRIO scanner (Siemens Healthcare, Erlangen, Germany) using a 32-channel RF coil (Siemens). Field maps were acquired with a dual-echo (TE = 5, 9 ms) GE sequence with TR = 950 ms, FA =  $25^\circ$ , and fat saturation (53 ACPC axial slices of 2 mm thickness with 0.3 mm gap,  $128 \times 128$  matrix, field of view 256 mm), pixel bandwidth = 260 Hz, and generalized autocalibrating partially parallel acquisition (GRAPPA) factor 2. Single-instance GE-EPIs with an effective echo time of 44 ms were acquired in the same geometry, with a receiver bandwidth of 1628 Hz/pixel.

#### Data Acquisition, 7 T

The same subject who was participated in the 3 T study was also scanned with a 7 T Magnetom MR whole body system (Siemens Healthcare, Erlangen, Germany) using an 8-channel RF coil (RAPID Biomedical, Würzburg, Germany), a 24-channel RF coil (Nova Medical, Wilmington), and a 32-channel RF coil (Nova Medical). Field maps were acquired with a dual-echo (TE = 5, 10 ms) GE sequence with TR = 1010 ms, FA =  $30^\circ$ , and fat saturation (53 ACPC axial slices of 2 mm thickness with 0.3 mm gap,  $128 \times 128$  matrix, field of view 256 mm), pixel bandwidth = 260 Hz, and GRAPPA factor 2. Single-instance GE-EPIs were acquired in the same geometry, with an effective echo time of 23 ms, GRAPPA factor 2, with partial Fourier encoding (omission of the first 25% of PE steps), with a receiver bandwidth of 1220 Hz/pixel.

#### Generation of Phase Maps From Multichannel Data

In the following subsections, we describe the generation of field maps with three methods: the HP method, based on the combination of both echoes and all channels into a single phase difference map via calculation of the sum Hermitian inner product (24); the phase-matching method (PM),

based on phase matching at each echo time using a reference region (10), and a separate channel (SC) method, based on phase difference images calculated from each channel separately. These three methods are described using the following general scheme: (i) generation of phase images or phase difference images, (ii) phase unwrapping, (iii) correction for  $n2\pi$  phase jumps between slices and echoes, (iv) conversion to field map, (v) noise reduction and (vi) local thresholding of the field map to yield the maximum achievable distortion correction. The main differences between the methods are related to the generation of the phase images from the multichannel data, as schematically illustrated in Fig. 1, the occurrence of phase unwrapping errors at low SNR and the possibilities for noise reduction. Thresholding the remapping gradient for EPI distortion correction is presented as an adjunct that can be applied to field maps calculated with any of these methods.

#### Generating Phase Difference Images From Multichannel Data

##### Calculation of Phase Difference Maps Using the HP

If the complex image for the  $l$ th channel at the first echo time is denoted  $S_{1,l}$  and that at the second echo time  $S_{2,l}$ , then the weighted mean phase difference  $\Delta\theta_{HP}$  can be calculated via the sum over channels of the Hermitian inner product (14,24,31,32)

$$\Delta\theta_{HP} = \text{angle} \left( \sum_l S_{2,l} S_{1,l}^* \right), \quad [1]$$

where  $S_1^*$  denotes the complex conjugate of  $S_1$ . Channel-specific phase offsets are removed by calculation of the differences in this method.

##### Calculation of Phase Maps Using the PM Method

In the PM method, combined phase images are calculated at each echo time, assuming that channel-specific phase offsets are constant for each channel  $l$  ( $\theta_{RX,l}$ ) and that this may be determined in a correction region of interest (cROI)—a number of pixels at the image center (10).

The corrected complex phase images at the first and second echo times  $S_{1,l}$  and  $S_{2,l}$  are given by

$$S_{1,l} = M_1 e^{i(\theta_1 - \theta_{RX,l})}, \quad [2]$$

and

$$S_{2,l} = M_2 e^{i(\theta_2 - \theta_{RX,l})}, \quad [3]$$

where  $M_1$  and  $M_2$  are the magnitudes at the respective echo times, and  $\theta_1$  and  $\theta_2$  the phases. The scalar phase corrections for both the first and second echoes,  $\theta_{RX,l}$ , are derived from the phase image at the first echo time.

The weighted PM image at the first echo,  $\theta_{wm-1}$ , is given by

$$\theta_{wm-1} = \text{angle} \left( \sum_l S_{1,l} \right), \quad [4]$$

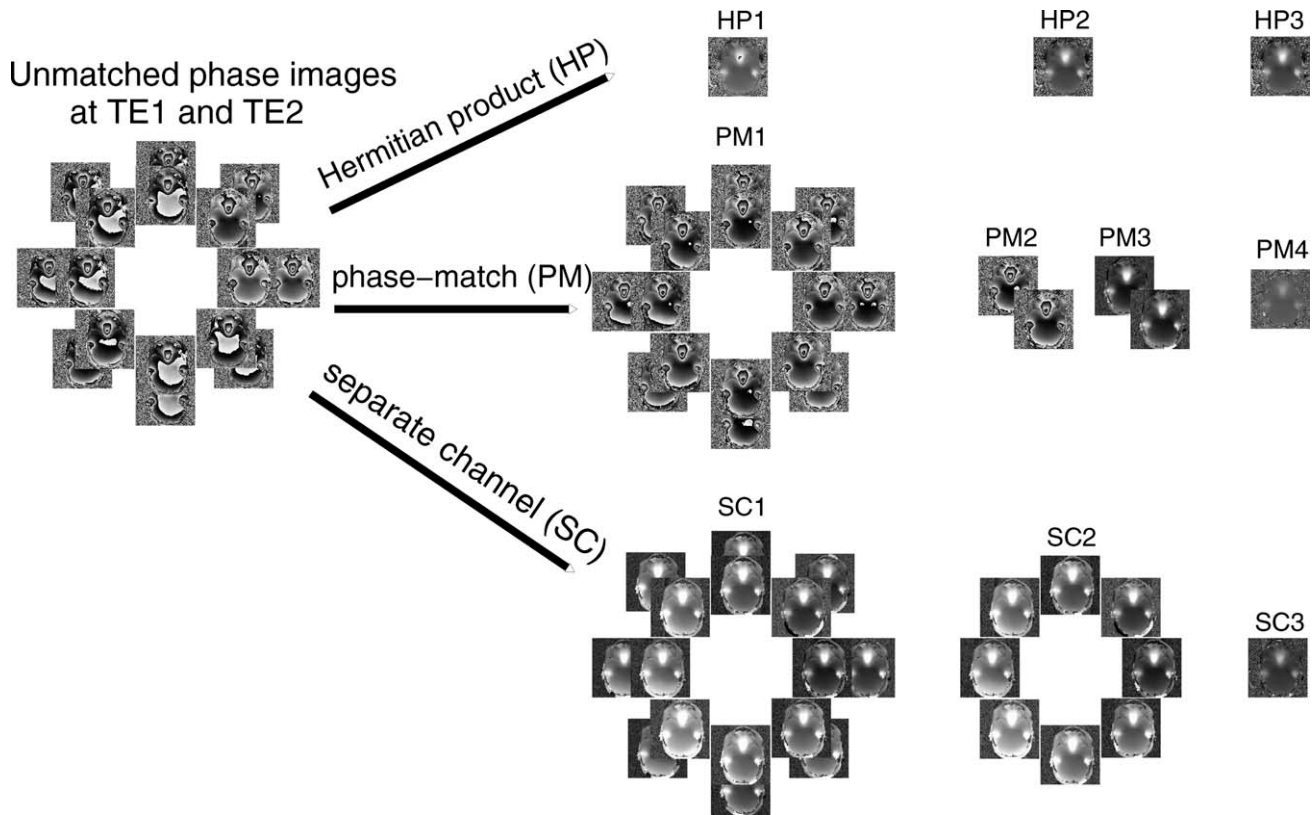


FIG. 1. An overview of the three field mapping methods being compared (for 8-channels). In the HP method, a phase difference image (HP1) was calculated according to Eq. 1. This was unwrapped (HP2) and the field map calculated (HP3). In the PM method, each channel phase was equalized in a cROI according to Eqs. 2 and 3 (PM1) before combining data from SCs, according to Eqs. 4 and 5, to yield a phase image at each echo time (PM2). These were unwrapped (PM3) and the field map calculated (PM4). In the SC method, phase images at echo time and for each channel were unwrapped (SC1) prior to calculating field maps for each channel (SC2) and combining these, via a trimmed weighted mean, to a single field map (SC3).

and that at the second,  $\theta_{wm_2}$

$$\theta_{wm_2} = \text{angle} \left( \sum_l S_{2,l} \right). \quad [5]$$

### Calculation of Phase Maps Using the SC Method

In the SC method, phase images for each channel and each echo are unwrapped separately. Jumps of  $n2\pi$  jumps between slices and echoes were identified and corrected (see below), and phase difference images (in rad) were calculated for each channel by subtracting values in the first unwrapped phase image from the second.

### Unwrapping phase images

Phase unwrapping was performed using PRELUDE v2.0 (18) from FSL ([www.fmrib.ox.ac.uk/fsl/](http://www.fmrib.ox.ac.uk/fsl/)). Processing was carried out on a PC with a quad-core 3.0 GHz Intel Xeon processor and 16 GB RAM with a 64-bit Ubuntu Linux operating system.

Two problems arise in phase unwrapping, and these affect the HP, PM, and SC methods differently. The first relates to unwrapping phase where SNR is low, such as in regions of signal dropout, the second to the occurrence of an integer number of  $2\pi$  phase jumps between slices and echoes.

Unwrapping algorithms may fail to identify phase wrap contours in the presence of noise, leading to artifacts manifesting as regions of residual phase difference. This problem was investigated with phantom measurements using a low flip angle acquisition and, for in vivo data, by adding Gaussian-distributed white noise to phase and magnitude data. In the phantom data, field map noise was assessed in ROIs in which no gross phase-mapping errors were present. The standard deviation of voxel values in these ROIs was compared between these methods with Students' paired two-tailed *t*-tests.

Phase unwrapping is a region-growing method which begins from a seed voxel, which should be chosen in a region of low phase gradient inside the object. The seed voxel is selected via an image property such as local coherence (33). If conducted in 2D mode, a seed voxel is selected in each slice. If there are  $n$  phase wraps between seed voxels in adjacent slices, phase values in voxels in the respective slices will differ by  $n2\pi$  in addition to the true phase difference between them. In the PM and SC methods, the same problem arises if there are  $n$  phase wraps between seed voxel locations in the raw (wrapped) phase images acquired at TE1 and TE2. These were corrected as follows.

- Phase inconsistencies between slices: subsequent to phase unwrapping with PRELUDE,  $n2\pi$  phase jumps

between slices were corrected, as follows, beginning at the central slice in the volume. Masks, calculated from magnitude images using FSL's Brain Extraction Technique (BET) (34) with a fractional intensity threshold of 0.5, were used to define in-brain pixels. The value of  $n$  between the central slice and an adjacent slice was calculated as the mean in-brain phase value in the central slice minus the mean in-brain phase value in the adjacent slice, divided by  $2\pi$  and rounded down to the nearest integer. The value of  $n2\pi$  calculated was added to the adjacent slice. The algorithm moved to the next pair of slices and continued until the final slice had been corrected, then processed slices from the central slice to the first slice in the volume in the same way.

- Phase inconsistencies across echoes: the value of  $n$  was determined by calculating the mean in-brain phase value at the first echo time, subtracting the mean in-brain phase value at the second echo time, dividing by  $2\pi$  and rounding down to the nearest integer. It is assumed that, in a shimmed volume, the true phase difference between the mean phase values of images acquired at two echo times is closer to zero than  $2\pi$ .  $n2\pi$  was subtracted from phase images at the second echo time.

#### Field map calculation, denoising, and consistency evaluation

Field maps were calculated from phase difference images via

$$B_0 = -\frac{\Delta\theta}{\gamma\Delta TE}, \quad [6]$$

and masked using the generous (tendentially large) masks calculated from magnitude images with BET. For the HP and PM methods, the phase differences are given by Eqs. (1) and (4), (5), respectively. For the SC method, a trimmed weighted mean field map was calculated over channels: the lowest and highest quartile field map values for each voxel were excluded and the weighted mean of the remaining values (equal in number to half the number of channels) was calculated, where the weights were corresponding magnitude images.

#### Field map denoising

As difference images, field maps are prone to noise, particularly at the object periphery. If they are to be used in distortion correction, field maps need to be masked to remove background noise and signal from the scalp, and unreliable voxels need to be identified and replaced by zero (if outside the brain) or reliable estimates. Masking, dilating, and smoothing (1), 2D median filtering (3), and three-dimensional Gaussian smoothing (31,35) have all been applied in this context. At high field strength and with multichannel receivers, transmit and receive  $B_1$  inhomogeneities lead to inhomogeneities in image intensity, which make the automatic identification of the brain-background boundary problematic. To circumvent this problem, we used only conservative masking, with BET,

followed by a number of noise reduction approaches: smoothing with a 6 mm full width half maximum (FWHM) Gaussian kernel, median filtering, and outlier filtering (replacement of the highest and lowest  $x\%$  of values by the median of  $5 \times 5$  voxel non-zero nearest neighbors, with  $x = 1, 5, 10,$  and  $30\%$ ). For the SC method, the additional possibility of identifying unreliable voxels using the standard deviation over channels was also tested.

The effect of distortion correcting EPI runs containing head motion on time-series SNR was evaluated, using field maps calculated with the HP, PM, and SC methods without any thresholding for the voxel-shift maps (4 T, 8-channel data).

#### Consistency between field maps

Consistency between field maps calculated with the HP, PM, and SC methods was assessed. The PM method is the only method that requires a cROI, and the robustness of the method to the criteria for its selection was assessed in problematic cases.

The cROI suggested by Hammond et al. uses an unspecified number of pixels at the center of the image (10). Schäfer et al. have noted that phase matching is not achieved using this cROI selection criterion if—because of the shape of the imaged object or its position in the coil—there is little or no signal at the center (11). We investigated a number of cROIs, which may, in general, appear in the image center. cROIs were selected, by deliberate placement in (1) a “Noise cROI”—a region in which there was little or no signal in all channels (11) (2) a “Wrap cROI”—a region (in this case in the orbitofrontal cortex) in which the cROI contained wraps in a number of channels (3) a “Disconnected cROI” in a region in which the signal was not connected to signal in the main image (chosen in one eyeball), and (4) a “Good cROI”—a region that was not affected by these problems. For each case, a  $3 \times 3 \times 3$  voxel cROI was used for phase matching.

#### Generation of Voxel Shift Maps for Distortion Correction

In the distortion correction process, field maps are converted, via the bandwidth per pixel in the phase-encode direction ( $RBW_{PE}$ ), to a voxel shift map (VSM). This defines the shift in the PE direction (a number of voxels) to be applied to each voxel in the distorted EPI to move signal to the correct position. Conflicts arise in this unwarping process if the magnitude of the gradient in the VSM in the phase-encode direction exceeds 1. At the limiting gradient value of 1, signal “pile-up” occurs, in which signal from a number of voxels is remapped to the same location, leaving voids that have to be filled with interpolated values. If the magnitude of the gradient of VSM exceeds 1, signal is swapped along the line of the correction. For instance, if  $j$  is the voxel index along the PE axis and  $VSM(j) = 3.1$  and  $VSM(j + 1) = 1.4$ , signal from voxel ( $j$ ) is remapped to voxel ( $j + 3.1$ ), and signal from ( $j + 1$ ) is remapped to ( $j + 2.4$ ). That is, the order of signal from ( $j$ ) and ( $j + 1$ ) is swapped along the PE axis. This leads to ring artifacts. Such conflicts can be avoided if the gradient in VSM in the PE direction is thresholded

at a value less than or equal to 1, which we will call  $\Delta VSM_{th}$ . Thresholding the VSM gradient leads to shifts that are lower than required for a complete correction but avoid the incurrence of pile-up artifacts.

The field map,  $B_0$ , is related to the VSM by

$$VSM = \frac{B_0}{RBW_{PE}}, \quad [7]$$

where  $B_0$  and  $RBW_{PE}$  are in the same units. If the field map  $B_0$  has indices (ro, pe, ss) in the readout, phase-encode and slice-select directions, respectively, with the corresponding matrix sizes (RO, PE, SS) then the amount by which the magnitude of the gradient of the VSM,  $\Delta VSM$ , exceeds the threshold, which we shall call  $\Delta VSM_{excess}$ , is given by

$$\begin{aligned} \Delta VSM_{excess} &= 0 & -\Delta VSM_{th} \leq \Delta(VSM) \leq \Delta VSM_{th} \\ \Delta VSM_{excess} &= \Delta(VSM) - \Delta VSM_{th} & \Delta(VSM) > \Delta VSM_{th} \\ \Delta VSM_{excess} &= \Delta(VSM) + \Delta VSM_{th} & \Delta(VSM) < -\Delta VSM_{th} \end{aligned} \quad [8]$$

and the map of the maximum resolvable voxel shift,  $VSM_{ms}$ , is

$$VSM_{ms}(ro, pe, ss) = VSM(ro, pe, ss) - \sum_0^{pe} \left( \Delta VSM_{excess} - \frac{\sum_0^{PE} (\Delta VSM_{excess})}{NNZ(\Delta VSM_{excess})} \right), \quad \Delta VSM_{excess} \neq 0 \quad [9]$$

where  $NNZ(\Delta VSM_{excess})$  is the number of non-zero elements in  $\Delta VSM_{excess}$ . The maximum resolvable VSM, described by Eq. 9, is reduced by both the local excess and the cumulative excess along the PE direction. This is so that if voxels shifts are reduced over a portion of a PE line they are increased afterwards to arrive at the same cumulative shift value. The rate of increase is given by the VSM threshold. If the cumulative shift were not considered, a local reduction in the VSM over a portion of the PE line would lead to a general reduction in the amount of shift for all points further along the PE line.

The distortion correction was performed with FSL's FUGUE, the first step of which is to "forward warp" the field map to match it to the EPI. This provides the remapping values for the distortion correction, and ensures that the field map relates to the appropriate part of the image (also, but not only, at the edge). For this reason, as long as the field map extends to the edge of the brain, geometric differences between the field map and EPI that come from distortion do not pose a problem in the distortion correction process.

To demonstrate the remapping artifacts and how these can be reduced by thresholding the gradient in the VSM, we carried out evaluations with both gradient-echo and spin-echo EPI data (4 T, 8-channel). Spin-echo EPI data suffers reduced signal dropout, so is expected to show more clearly the remapping artifacts and how they are alleviated.

To compare the performance of field map corrections with HP, PM, SC, and SC with VSM gradient thresholding, the correlation ratio was calculated between distortion-corrected EPIs and anatomical GEs (illustrated in the far right column of Fig. 5). Correlation ratio is a cost function commonly used in assessing congruence between images (e.g., in FSL's image registration tool, FLIRT (36)), and was calculated using the MATLAB "corrcoef" function. The fractional increase in correlation with GEs was calculated by dividing correlation ratios for distortion-corrected images by the correlation between raw EPIs and anatomical GEs.

## RESULTS

### Comparison of Methods for Generating Phase Difference Images From Multichannel Data

The PM method is the only method to require a correction region. Irresolvable phase irregularities appeared using the Noise cROI and the Wrapped cROI (Fig. 2, at arrow positions). No such irregularities were generated when using a disconnected cROI or a good cROI.

In high SNR regions, there was broad agreement between phase difference images calculated with the HP, PM, and SC methods. Figure 3 illustrates the correction of phase jumps across slices.

In summary, with high SNR images and  $n2\pi$  phase jump correction across slices and echoes, the HP, PM, and SC methods generated comparable phase difference images provided that the PM correction region was not noisy or wrapped.

### Phase Unwrapping Errors at Low SNR: Effect of Coil Combination Method

Phase unwrapping errors occurred at low SNR, and the frequency and severity of these was dependent on whether phase data were combined with the HP, PM, or SC method. For in vivo field map data to which noise had been added (Fig. 4), HP field maps suffered from isolated wrapped and zero pixels in-brain (arrows pointing up), and unwrapping errors in frontal and temporal regions (arrows pointing down). There were no in-brain isolated pixel errors with the PM method, but unwrapping errors were more frequent than with either the HP or SC methods (arrows pointing down, Fig. 4). SC field maps were least prone to errors. The background is more uniform in the SC method as—with noise having been added to these data—some background voxels were below the threshold for unwrapping.

The phantom data likewise showed that most errors were encountered with the PM method, followed by the HP method (results not shown). While unwrapping errors occurred in single-channel data, these were removed by the calculation of the trimmed weighted mean in the SC method. Field map noise was lowest in the SC method (HP:  $263 \pm 36$ , PM:  $279 \pm 26$ , SC:  $228 \pm 33$ , rad/s units). At the  $P < 0.05$  level, field map noise was significantly lower in the SC method than the PM method ( $P = 0.0153$ ,  $t = 2.92$ , 10 dof) but not significantly lower than in the HP method ( $P = 0.121$ ,  $t = 1.69$ , 10 dof). There was no significant difference between the

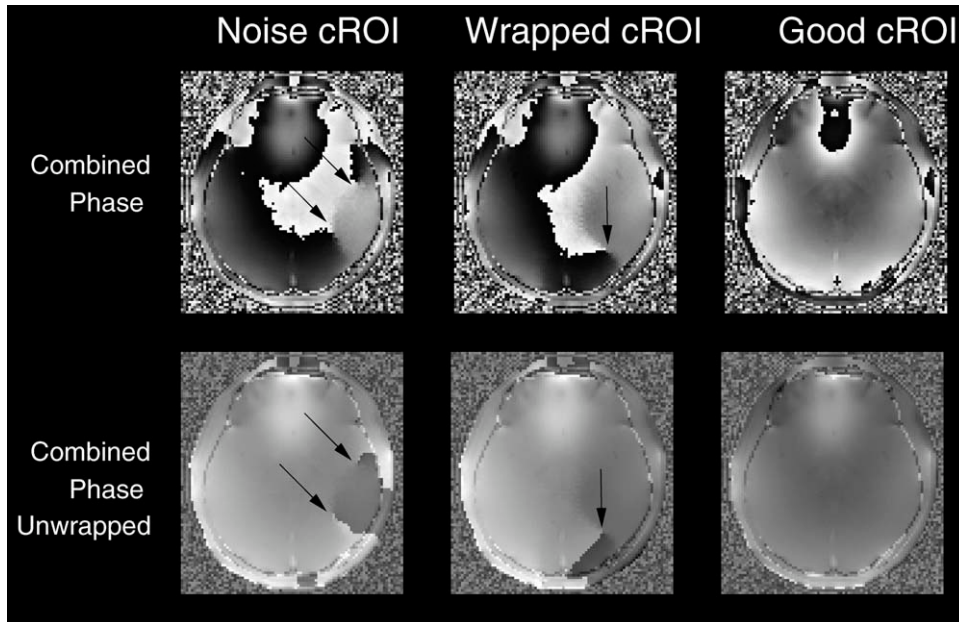


FIG. 2. Artifacts in combined phase images in the PM method when the correction ROI lies in a region of noise (left column), encompasses a phase wrap (center column), or has both high SNR and no phase wraps (right column). Arrows indicate irresolvable phase irregularities.

HP and PM methods ( $P = 0.389$ ,  $t = 0.901$ , 10 dof). To summarize, the SC method yielded the most robust field maps under low SNR conditions.

#### Reliability of Methods With Number of Channels and Field Strength and Denoising of Field Maps

Generalization of the field mapping methods to various hardware configurations was evaluated by applying the methods to sample data acquired at a range of field strengths and with phased array coils with different numbers of receiver elements (Fig. 5). Contours at the anterior edge of the brain and the border of frontal grey and white matter were traced on GE reference scans by hand (Fig. 5, far right column, in yellow) and transferred to EPIs to illustrate the extent of distortion in raw EPI (far left column) and the quality of correction in the HP and SC approaches.

The HP method requires the unwrapping of phase difference images, which have lower SNR than non-difference images. These field maps show some unwrapping errors within the brain (arrows pointing right), particularly in the basal ganglia and other short  $T_2^*$  regions. Sim-

ple smoothing with a Gaussian kernel led to the perpetuation of noisy edge voxels. Median filtering also led to unsatisfactory results, with small kernels giving noisy edges, and large kernels smoothing field maps to an extent that they failed to accurately restore EPI shape. HP field maps in Fig. 5 were outlier denoised, with the 5% of most extreme values being replaced by the median of non-zero nearest neighbors in a  $5 \times 5$  voxel square. This removed much of residual streaking artifacts, though some unreliable field map values remained. Arrows pointing left in Fig. 5 indicate noisy edge voxels in HP field maps, and corresponding irregularities in corrected EPI compared to GE reference images. Results for the PM method were similar to those for the HP method. Standard deviation denoising was only possible with the SC field maps, because it is the only approach for which there are a number of field map values for each voxel.

For the SC method, reliable field maps could be calculated for all coils and field strengths using the following consistent criteria. For the brain extraction the default BET threshold of 0.5 was used. The number of channels included in a trimmed weighted mean was set to half the total number of channels, with the upper and lower

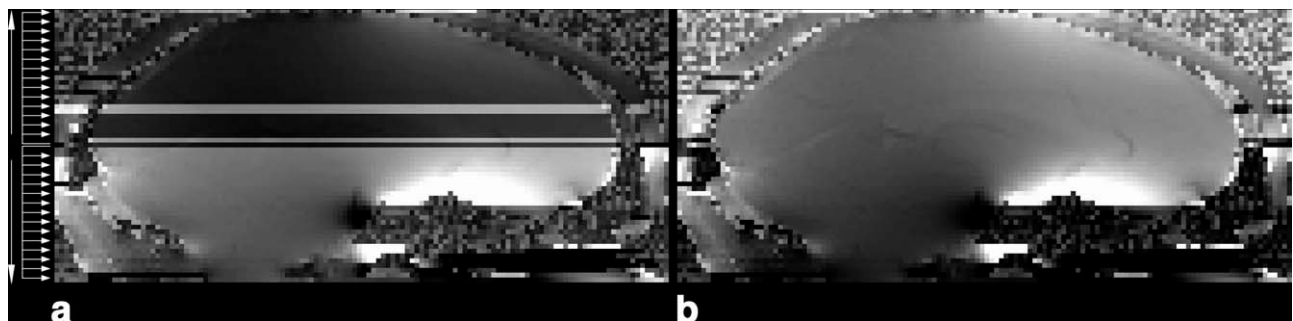


FIG. 3. Correction of  $n2\pi$  phase jumps between slices. (a) Axial phase difference images unwrapped in 2D contain  $2\pi$  phase jumps between slices which were removed using the method described in the text. (b) The slice order for correction is indicated in arrows on the left.

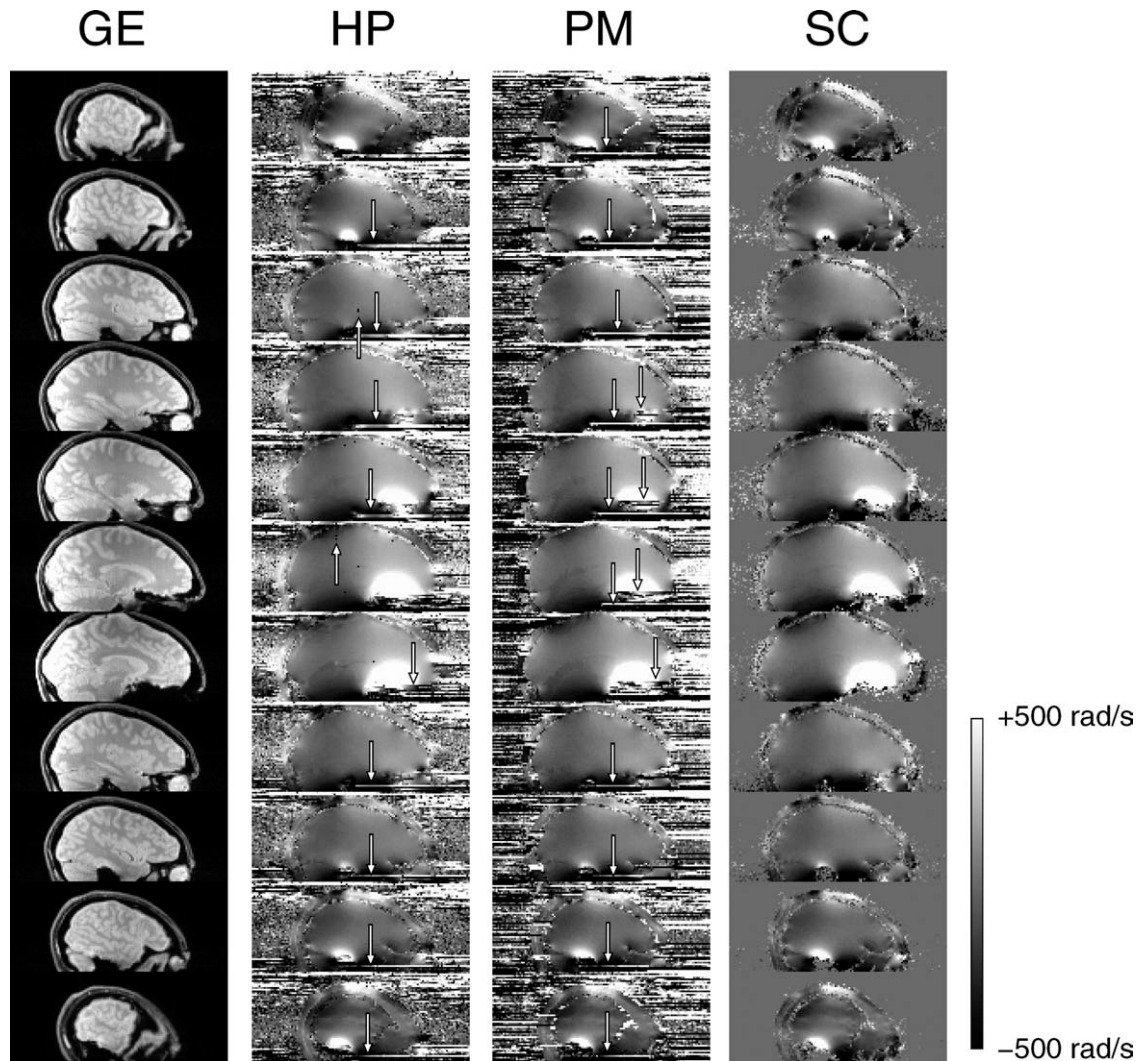


FIG. 4. Field maps derived from low SNR phase images (4 T, 8-channel field map data with 15% gaussian-distributed white noise added). Sensitivity to unwrapping errors for the different methods for combining multi-channel data: HP, PM, and SC methods. No masking or denoising was applied. Arrows pointing up indicate isolated voxel unwrapping errors, those pointing down indicate unwrapping errors over large regions.

quartile values for each voxel being rejected. Field map denoising was achieved via the standard deviation threshold across channels. Pixel values in which the standard deviation was more than three times the median, in-brain standard deviation were replaced by the median of non-zero nearest neighbors in a  $5 \times 5$  voxel square. With these criteria there is consistently good correction of EPI over channels and field strengths when comparing with the gradient-echo reference (Fig. 5), even for the greatest EPI distortion (4 T, without parallel imaging).

To summarize, our results show that the three phase-mapping methods evaluated can be generalized to a wide range of MRI hardware configurations of field and multichannel RF coils.

#### Field Map Distortion Correction: Thresholding VSMs

Figure 6 illustrates areas in which high gradients in VSMs lead to artifacts (GE-EPI, 4 T, 8-channel data) and how these are avoided by the thresholding proposed.

Artifacts can be seen in corrected EPI, second from left (regions outlined in yellow). Thresholding the maximum gradient in the VSM removed the occurrence of these artifacts (bottom row, second from right) at the expense of an incomplete correction in those regions. The thresholding is based on local gradient, meaning that the distortion correction is unaffected in other regions. For instance, the remapping is approximately 8 mm in the region of the brain stem in both the gradient-thresholded and unthresholded VSMs (Fig. 6, red crosses), and the correction can be seen to be accurate when compared with the distortion-free reference scan.

In gradient-echo EPI, some of the largest distortions occur in regions with substantial signal dropout. We also evaluated remapping errors in SE-EPI (4 T, 8-channel), where the pile-up artifact is pronounced due to refocusing of signal in regions of strong static susceptibility gradients (Fig. 7), and assessed the effect of the correction on fMRI data quality in time-series EPI containing motion. Remapping artifacts arising from high

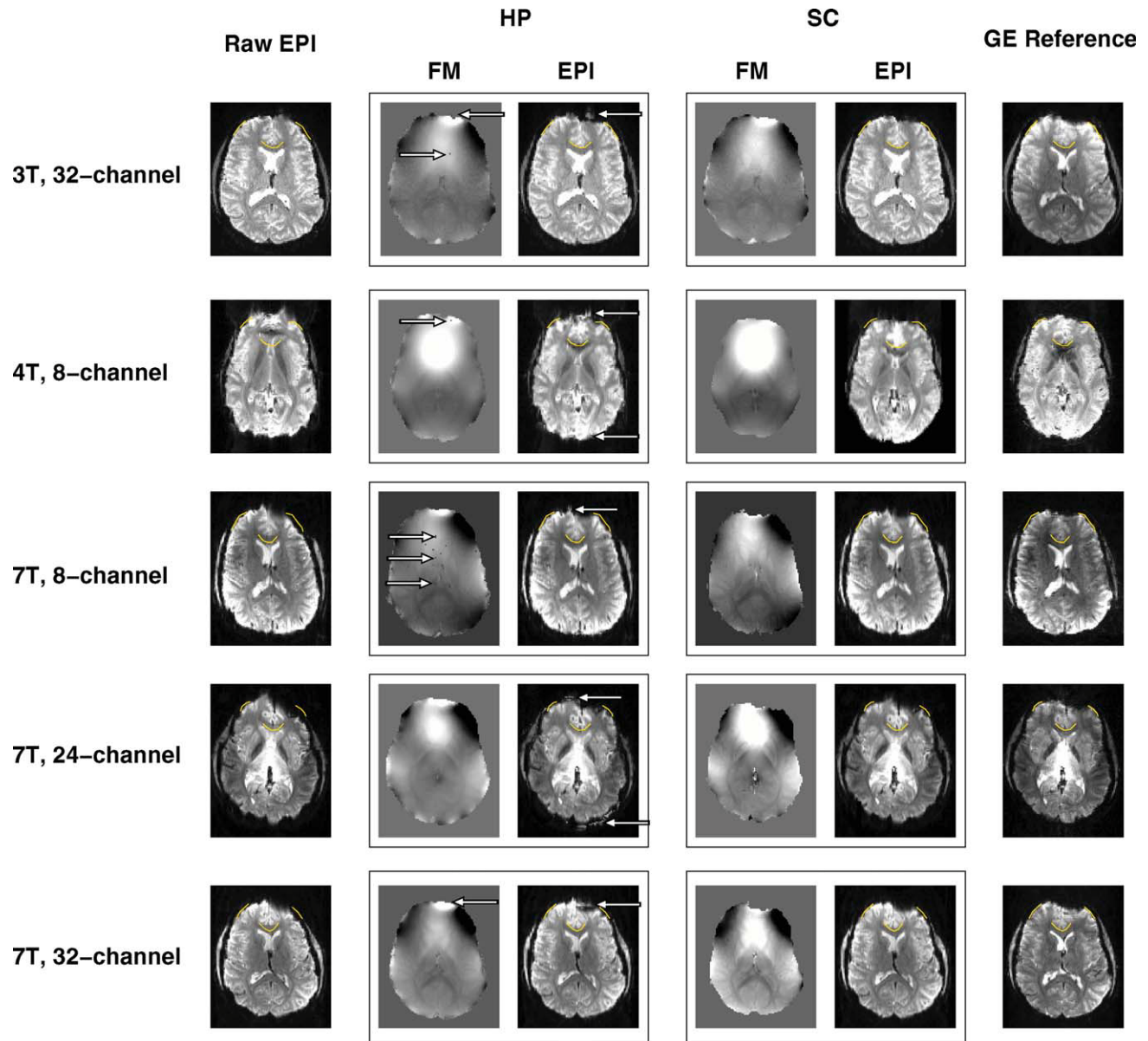


FIG. 5. Multichannel field maps derived from measurements made with a range of number of channels at 3 T, 4 T, and 7 T, and corresponding EPI distortion corrections. Some unwrapping errors are apparent with the HP method (arrows pointing right). Outlier denoising (5%) was used for HP field maps. For SC field maps, unreliable voxels in trimmed weighted mean field maps were identified via the standard deviation over channels. Arrows pointing left indicate noisy edge voxels in HP field maps and corresponding irregularities in corrected EPI compared with gradient-echo reference images. Yellow contours traced manually on the GE reference scan are overlaid on the EPI data (see text for more details). [Color figure can be viewed in the online issue, which is available at [wileyonlinelibrary.com](http://wileyonlinelibrary.com).]

gradients can be clearly seen when comparing raw SE-EPI data (Fig. 7, first row) with the distortion corrected data, where no gradient thresholding was applied (Fig. 7, second row, at arrow positions). Remapping artifacts are visibly reduced by thresholding the gradient in the VSMs (to 0.8) (Fig. 7, third row). The effects of voxel shift thresholding were also evaluated in terms of time-series SNR in an acquisition with head motion. FSL's MCFLIRT (36), which was used quantify the extent of motion but not to motion-correct the time series, identified a continuous rotation about the  $y$  axis of the scanner of 0.5 degrees from beginning to end. As can be seen in Fig. 7 (bottom row), time-series SNR in the gradient-

thresholded series is much higher in the region affected by the artifact (in the unthresholded series) and unchanged in the rest of the brain. There are no significant differences in slices superior to those shown.

The time taken to calculate denoised and thresholded field maps was 56 s for the HP method (with outlier denoising), 1 min 36 s for the PM method (with outlier denoising) and 3 min 22 s for the SC method (with standard deviation denoising).

The quality of the field map-based distortion correction with the HP, PM, and SC methods was evaluated via the percentage increase in the correlation between field map corrected EPI and reference GE over the

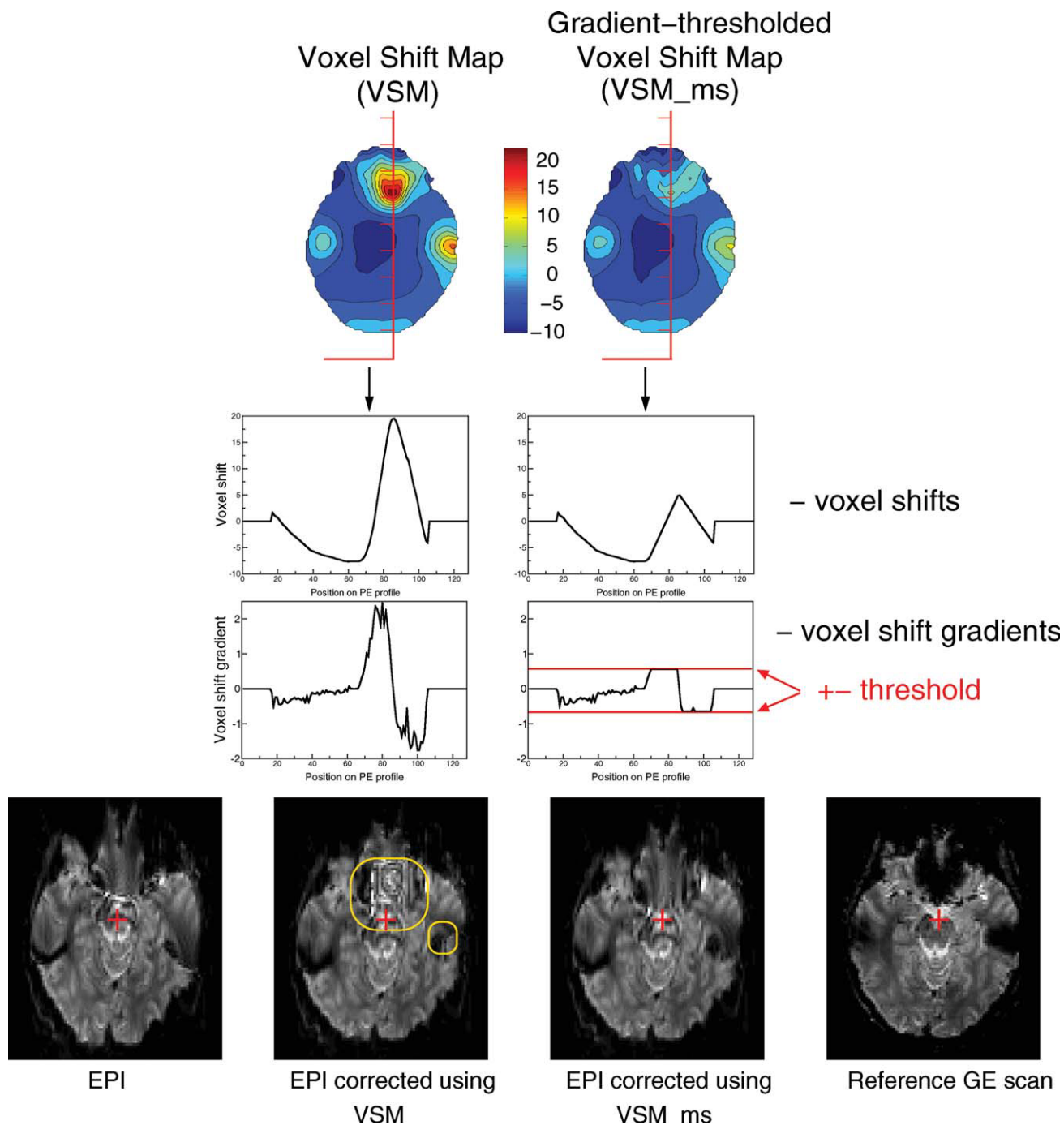


FIG. 6. Thresholding the maximum gradient in voxel shifts maps derived from field maps removes artifacts due to voxel remapping conflicts (regions in yellow boxes). The distortion correction remains effective in regions with lower field gradient. The 8 mm correction needed close to the brain stem (red cross positions in the first and second columns) is maintained in the VSM thresholded correction (third column).

correlation value between raw EPI and reference GE. Figure 8 illustrates this metric as a function of RBW, which is inversely proportional to distortion. Gradient thresholding was applied to the SC method only and is plotted separately (“SC\_thresh”). Values are averages over all subjects scanned at 4 T. The trend over a range of distortions is that SC field maps yielded better results than HP and PM, which differed little. Gradient thresholding gave an additional increase in correlation

with reference GE at most values of RBW. There are fluctuations as a function of RBW that are similar for all methods (e.g., the maximum in all methods is at 1150 Hz/pixel). The shape of the similarity measure as function of RBW is the result of the combination of factors that change with RBW, including: image distortions (which decrease with increasing RBW), Nyquist ghosts (which tend to have peaks at the acoustic resonant frequencies of the scanner) and SNR (which decreases with increasing RBW).

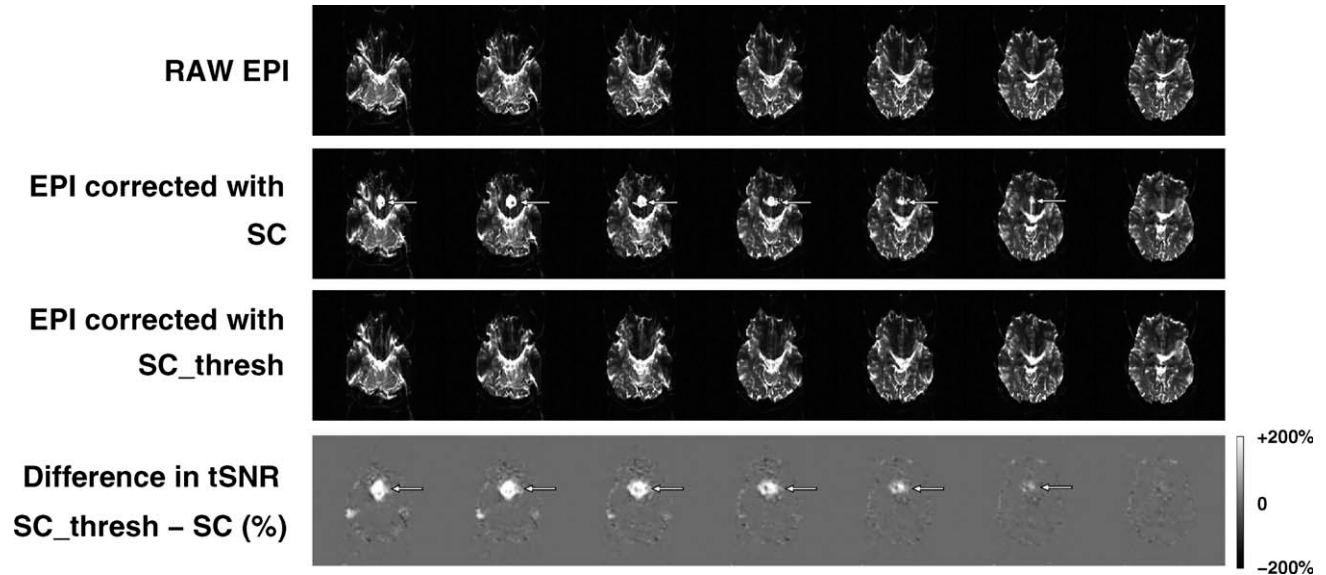


FIG. 7. Correcting raw EPI (top line) without thresholding the fieldmap generates signal pile-up artifacts in regions where the gradient in voxel shifts exceeds the value of 1 (at arrow positions in the second row). Thresholding the maximum voxel shift gradient avoids the occurrence of this artifact (third row). In the presence of head motion, time-series SNR is much higher in EPI data that was corrected with thresholded field maps than without the gradient thresholding (bottom row). The data shown correspond to spin-echo EPI (4 T, 8-channel).

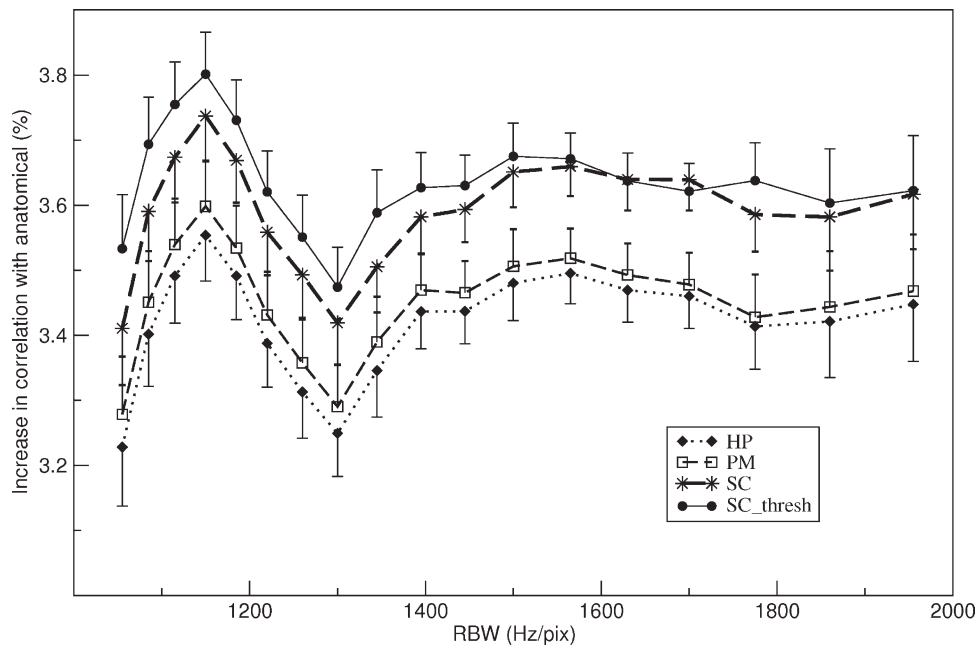


FIG. 8. Distortion correction effectiveness of the field mapping approaches tested (HP, PM, SC, and SC including gradient thresholding). The correlation between EPI corrected with each method and the reference anatomical gradient-echo image was compared with the correlation ratio between raw distorted EPI and the anatomical reference to yield the fractional increase in correlation. More than six subjects over the whole imaged volume were analyzed (4 T, 8-channel). For clarity, half-errors are shown.

**DISCUSSION**

Three methods for combining phase images from multi-channel coils were implemented and assessed, examining robustness in the calculation of phase images, unwrapping errors at low SNR and field map denoising possibilities. Simple, effective methods are presented for the correction of interslice and interecho phase jumps

and for the thresholding of VSMs to the maximum achievable field map-based distortion correction. The comparison of the methods was done mainly using a 4 T (8-channel) MR configuration in a group of subjects. The generalization of the methods is also demonstrated for other hardware configurations, namely 3 T (32-channel coil) and 7 T (8-channel, 24-channel, and 32-channel coil).

Two of the phase combination methods examined, the HP and PM methods, have been presented previously in the literature (Refs. 10 and 24, respectively). The method proposed here, which is based on calculating separate field maps for each channel separately and combining these (SC), was found to have two major advantages over the HP and PM methods. First, the SC method was less prone to unwrapping errors at low SNR, as errors are effectively excluded in the trimmed weighted mean over channels. Second, reduction of noise in field maps via the standard deviation over channels, possible in the SC method but not in the other two methods, was found to be superior to methods based either on spatial variation in field maps (e.g., median filtering) or by outlier identification, as some reliable field map values lie at the extremes of the distribution, and some noise values do not. As a result, even the most dramatic outlier thresholding tested (replacing the top and bottom 30% of values) left unreliable voxels, as well as reducing the correction magnitude in regions where field values were large, but valid. In the SC method, noise in the combined field map could be kept low by including in a trimmed weighted mean, only the middle 50th percentile of phase values for each voxel. Residual noise in the masked, combined field map could be effectively reduced using the standard deviation over channels, where the standard deviation threshold for unreliable voxels could be determined from the range of standard deviation values in the image: three times the median value was found to yield good results for all coils, field strengths, and subjects. Even outside the regions where these artifacts were present in the HP and PM methods, field maps calculated with the SC method showed the lowest noise (significantly lower than the PM method). As an additional advantage over the PM method, the SC approach does not depend on a correction region. The PM method was found not to achieve adequate phase matching if the correction region lay in noise, and if it contained phase wraps—both of which problems can occur in automatic selection criterion (10). A recent study into phase combination methods demonstrated that the PM method can lead to regions of complete signal cancellation in high field, high-resolution acquisitions with RF coils with a large number of elements (13). This problem was not observed here because of the much lower resolution.

We have proposed a means to identify the maximum remappable voxel shift; where the gradient in the VSM in the PE direction is equal to 1. At voxel shift gradients higher than this, signal is reordered along PE lines, leading to artifacts in EPI and low time-series SNR if there is motion during an fMRI run. A small degree of correlation of motion with the stimulus could also lead to artifactual activation (37) in fMRI studies in regions of high field gradients, as has been demonstrated for the amygdala (38). While the reduced correction in these regions is inadequate to fully restore the true shape of the brain, it represents the largest degree of correction possible, and reduces the sensitivity of the correction process to small motion between acquisition of the reference scan and EPI. Modifying the field map so that the maximum value of the gradient in the VSM gradient was below 1 was shown to be sufficient to provide some distributed signal

for interpolation, and the correction was complete in other regions of the brain. Summarizing, thresholding the gradient in the VSM has two main advantages relative to not thresholding: higher similarity to the anatomical reference and higher time-series SNR.

The relatively low resolution of EPI and efficiency of modern unwrapping algorithms (33) means that even for the SC method, the most computationally intensive of those presented, complete processing of field maps from an 8-channel receive array takes approximately 3 min on a typical desktop PC.

## CONCLUSIONS

Two existing and one novel approach to calculating field maps from multichannel coils have been implemented and tested on 3 T, 4 T and 7 T scanners using head RF coils with between 8 and 32 receiving elements. The method introduced here, based on the calculation of field maps from separate channels, yielded field maps with higher SNR than the other methods and showed fewest unwrapping errors at low SNR. The SC method also allowed unreliable voxels to be identified via the standard deviation over channels, which was found to be the most effective means of denoising field maps. A common application of field maps is the correction of geometric distortions in EPI. A method for avoiding voxel remapping conflicts is proposed and demonstrated, based on the local thresholding of the VSM. This method has two main advantages: it improves the similarity of the distortion corrected EPI with the anatomical image and it increases time-series SNR compared to field map distortion correction without gradient thresholding, particularly in areas with strong magnetic field inhomogeneities. The methods described here have been implemented as a freely available MATLAB toolbox <http://www.mathworks.com/matlabcentral/fileexchange/30853-field-mapping-toolbox> and provide the framework for reliable field mapping and distortion correction at high field with multichannel coils.

## ACKNOWLEDGMENTS

The authors thank Andre van der Kouwe for providing the multi-echo FLASH sequence, originally developed at Massachusetts General Hospital, Boston, MA, which was used in the 4 T experiments.

## REFERENCES

1. Jezzard P, Balaban RS. Correction for geometric distortion in echo planar images from B<sub>0</sub> field variations. *Magn Reson Med* 1995;34:65–73.
2. Zeng H, Constable RT. Image distortion correction in EPI: comparison of field mapping with point spread function mapping. *Magn Reson Med* 2002;48:137–146.
3. Zaitsev M, Hennig J, Speck O. Point spread function mapping with parallel imaging techniques and high acceleration factors: fast, robust, and flexible method for echo-planar imaging distortion correction. *Magn Reson Med* 2004;52:1156–1166.
4. In M, Jung JY, Oh SH, Zaitsev M, Cho ZH, Speck O. Improved PSF-based EPI distortion correction in human imaging at 7 Tesla. Proceedings of the Eighteenth Meeting of the International Society for Magnetic Resonance in Medicine, Stockholm, Sweden, 2010.
5. Xiang QS, Ye FQ. Correction for geometric distortion and N/2 ghosting in EPI by phase labeling for additional coordinate encoding (PLACE). *Magn Reson Med* 2007;57:731–741.

6. Techavipoo U, Lackey J, Shi J, Leist T, Lai S. Phase labeling using sensitivity encoding (PLUS): data acquisition and image reconstruction for geometric distortion correction in EPI. *Magn Reson Med* 2009;61:650–658.
7. Weiskopf N, Hutton C, Josephs O, Deichmann R. Optimal EPI parameters for reduction of susceptibility-induced BOLD sensitivity losses: a whole-brain analysis at 3 T and 1.5 T. *NeuroImage* 2006;33:493–504.
8. Wiggins GC, Polimeni JR, Potthast A, Schmitt M, Alagappan V, Wald LL. 96-Channel receive-only head coil for 3 Tesla: design optimization and evaluation. *Magn Reson Med* 2009;62:754–762.
9. Wiggins GC, Triantafyllou C, Potthast A, Reykowski A, Nittka M, Wald LL. 32-channel 3 Tesla receive-only phased-array head coil with soccer-ball element geometry. *Magn Reson Med* 2006;56:216–223.
10. Hammond KE, Lupo JM, Xu D, Metcalf M, Kelley DA, Pelletier D, Chang SM, Mukherjee P, Vigneron DB, Nelson SJ. Development of a robust method for generating 7.0 T multichannel phase images of the brain with application to normal volunteers and patients with neurological diseases. *NeuroImage* 2008;39:1682–1692.
11. Schäfer A, Turner R. A general method for generating multichannel phase images without using a body coil. *ISMRM Workshop Series 2008: High Field Systems & Applications: "What's Special about 7T+?"*, Rome, Italy, 2008.
12. Roemer PB, Edelstein WA, Hayes CE, Souza SP, Mueller OM. The NMR phased array. *Magn Reson Med* 1990;16:192–225.
13. Robinson S, Grabner G, Witoszynskij S, Trattig S. Combining phase images from multi-channel RF coils using 3D phase offset maps derived from a dual-echo scan. *Magn Reson Med* 2011 [Epub ahead of print]. DOI: 10.1002/mrm.22753.
14. Scharnhorst K. Angles in complex vector spaces. *Acta Appl Math* 2001;69:95–103.
15. Duyn JH, van Gelderen P, Li TQ, de Zwart JA, Koretsky AP, Fukunaga M. High-field MRI of brain cortical substructure based on signal phase. *Proc Natl Acad Sci USA* 2007;104:11796–11801.
16. Koopmans PJ, Manniesing R, Niessen WJ, Viergever MA, Barth M. MR venography of the human brain using susceptibility weighted imaging at very high field strength. *Magn Reson Mater Phys* 2008;21:149–158.
17. Chen Z, Johnston LA, Kwon DH, Oh SH, Cho ZH, Egan GF. An optimised framework for reconstructing and processing MR phase images. *NeuroImage* 2009;49:1289–1300.
18. Jenkinson M. Fast, automated, N-dimensional phase-unwrapping algorithm. *Magn Reson Med* 2003;49:193–197.
19. Witoszynskij S, Rauscher A, Reichenbach JR, Barth M. Phase unwrapping of MR images using Phi UN—a fast and robust region growing algorithm. *Med Image Anal* 2009;13:257–268.
20. Reber PJ, Wong EC, Buxton RB, Frank LR. Correction of off resonance-related distortion in echo-planar imaging using EPI-based field maps. *Magn Reson Med* 1998;39:328–330.
21. Chen NK, Wyrwicz AM. Correction for EPI distortions using multi-echo gradient-echo imaging. *Magn Reson Med* 1999;41:1206–1213.
22. Windischberger C, Robinson S, Rauscher A, Barth M, Moser E. Robust field map generation using a triple-echo acquisition. *J Magn Reson Imaging* 2004;20:730.
23. Hutton C, Bork A, Josephs O, Deichmann R, Ashburner J, Turner R. Image distortion correction in fMRI: a quantitative evaluation. *NeuroImage* 2002;16:217–240.
24. Lu K, Liu TT, Bydder M. Optimal phase difference reconstruction: comparison of two methods. *Magn Reson Imaging* 2008;26:142–145.
25. Robinson S, Barth M, Jovicich J. Fast, high resolution T2\* mapping using 3D MGE and 3D EPI, with 3D correction for macroscopic dephasing effects. *Proceedings of the Seventeenth Annual Meeting of the ISMRM*, Toronto, Canada, 2009. p 4525.
26. Baudrexel S, Volz S, Preibisch C, Klein JC, Steinmetz H, Hilker R, Deichmann R. Rapid single-scan T2\*-mapping using exponential excitation pulses and image-based correction for linear background gradients. *Magn Reson Med* 2009;62:263–268.
27. Dahnke H, Schaeffter T. Limits of detection of SPIO at 3.0 T using T2 relaxometry. *Magn Reson Med* 2005;53:1202–1206.
28. Bandettini PA, Wong EC, Jesmanowicz A, Hinks RS, Hyde JS. Spin-echo and gradient-echo EPI of human brain activation using BOLD contrast: a comparative study at 1.5 T. *NMR Biomed* 1994;7:12–20.
29. Schmidt CF, Boesiger P, Ishai A. Comparison of fMRI activation as measured with gradient- and spin-echo EPI during visual perception. *NeuroImage* 2005;26:852–859.
30. Jovicich J, Norris DG. Functional MRI of the human brain with GRASE-based BOLD contrast. *Magn Reson Med* 1999;41:871–876.
31. Bernstein MA, Grgic M, Brosnan TJ, Pelc NJ. Reconstructions of phase contrast, phased array multicoil data. *Magn Reson Med* 1994;32:330–334.
32. Thunberg P, Karlsson M, Wigstrom L. Comparison of different methods for combining phase-contrast images obtained with multiple coils. *Magn Reson Imaging* 2005;23:795–799.
33. Witoszynskij S, Rauscher A, Reichenbach JR, Barth M. Phase unwrapping of MR images using Phi UN—a fast and robust region growing algorithm. *Med Image Anal* 2008.
34. Smith S. Fast robust automated brain extraction. *Hum Brain Mapp* 2002;17:143–155.
35. Jenkinson M. Improved unwarping of EPI images using regularised B0 maps. *NeuroImage* 2001;13:S165.
36. Jenkinson M, Bannister P, Brady M, Smith S. Improved optimization for the robust and accurate linear registration and motion correction of brain images. *NeuroImage* 2002;17:825–841.
37. Hajnal J, Myers R, Oatridge A, Schwieso J, Young I, Bydder G. Artifacts due to stimulus correlated motion in functional imaging of the brain. *Magn Reson Med* 1994;31:283–291.
38. Robinson S, Moser E. Positive results in amygdala fMRI: emotion or head motion? *NeuroImage* 2004;22 (Suppl 1):294.